Computational Modeling Predicts Immuno-Mechanical Mechanisms of Maladaptive Aortic Remodeling in Hypertension

Abstract

Uncontrolled hypertension is a major risk factor for myriad cardiovascular diseases. Among its many effects, hypertension increases central artery stiffness which in turn is both an initiator and indicator of disease. Despite extensive clinical, animal, and basic science studies, the biochemomechanical mechanisms by which hypertension drives aortic stiffening remain unclear. In this paper, we show that a new computational model of aortic growth and remodeling can capture differential effects of induced hypertension on the thoracic and abdominal aorta in a common mouse model of disease. Because the simulations treat the aortic wall as a constrained mixture of different constituents having different material properties and rates of turnover, one can gain increased insight into underlying constituent-level mechanisms of aortic remodeling. Model results suggest that the aorta can mechano-adapt locally to blood pressure elevation in the absence of marked inflammation, but large increases in inflammation drive a persistent maladaptive phenotype characterized primarily by adventitial fibrosis. Moreover, this fibrosis appears to occur via a marked increase in the rate of deposition of collagen having different material properties in the absence of a compensatory increase in the rate of matrix degradation. Controlling inflammation thus appears to be key to reducing fibrosis, but therapeutic strategies should not compromise the proteolytic activity of the wall that is essential to mechanical homeostasis.

Keywords: wall stress, blood pressure, aorta, constrained mixture, inflammation

1. Introduction

It has long been known that angiotensin II (AngII) plays diverse roles in arterial health and disease, particularly by affecting blood pressure regulation and hypertension. Bardy et al. (1996) showed, for example, that exogenous AngII and imposed increases in transmu-

ral pressures can independently stimulate extracellular matrix production within the aortic wall, the latter via wall stress / strain induced stimulation of a local renin-angiotensin system and signaling through the type 1 angiotensin receptor. These ex vivo findings were confirmed in vitro by Li et al. (1998) who showed that increased cyclic stretch / stress similarly increases matrix production by isolated vascular smooth muscle cells via local AngII production and associated increases in transforming growth factor-beta. Notwithstanding the utility of ex vivo and in vitro studies, the complex nature of the effects of AngII in hypertension demands further investigation and validation via in vivo experimental data. Toward this end, rodent models continue to be extremely valuable in elucidating underlying genetic, molecular, and mechanical mechanisms in cardiovascular disease. A commonly used animal model of induced hypertension involves the continuous infusion of AngII in mice. For example, Louis et al. (2007) demonstrated the importance of cellular mechanosensing in induced hypertension by contrasting effects of AngII infusion on the structure and mechanical properties of common carotid arteries from WT (wild-type) and $Itga1^{-/-}$ (integrin subunit alpha-1 null) mice. Tieu et al. (2009) used the AngII infusion model to show the importance of the pro-inflammatory cytokine IL-6 in promoting adverse macrophage-mediated aortic wall remodeling in induced hypertension by contrasting its effects in male WT, $Il6^{-/-}$ (interleukin-6 null), and $Ccr2^{-/-}$ (where the $Ccr2$ gene encodes a chemokine receptor for monocyte chemoattractant protein-1) mice. Wu et al. (2014) compared consequences of AngII infusion in male WT, immunocompromised $Rag1^{-/-}$ (lacking mature B- and T-lymphocytes), and $Il17a^{-/-}$ mice, and showed that T Helper 17 (Th17) production of the pro-fibrotic cytokine IL-17a drives adventitial fibrosis in the hypertensive thoracic aorta. Ji et al. (2014) showed further that sex-differences in AngII-induced hypertension depend strongly on differences in T-cell regulation of pro-fibrotic (IL-17a) and anti-inflammatory (IL-10) cytokines between males and females.

Hypertension often presents with co-morbidities, such as hyperlipidemia, which tends to increase the risk for development and progression of atherosclerosis. For this reason, effects of AngII infusion have also been commonly studied in either $Apoe^{-/-}$ (apolipoprotein-E null) or $Ldlr^{-/-}$ (low density lipoprotein receptor null) mice, both of which have a propensity for atherosclerosis that is exacerbated when placed on a high fat diet. We recently reported an

unexpected observation in AngII infused $Apoe^{-/-}$ mice maintained on a regular diet; namely, the infrarenal abdominal aorta (IAA) mechano-adapted while the descending thoracic aorta (DTA) maladapted within the same hypertensive animals (Bersi et al., 2017). In this regard, we define a local mechano-adaptation as a near restoration of both blood pressure-induced mean circumferential wall stress and blood flow-induced mean wall shear stress, which require locally that luminal radius $a \to \epsilon^{1/3} a_h$ and wall thickness $h \to \epsilon^{1/3} \gamma h_h$ (Humphrey, 2008) where ϵ and γ represent fold-changes in flow and pressure from homeostatic, which is denoted by subscript h. Importantly, the maladaptation within the thoracic aorta correlated strongly with increased inflammation, as measured by an increased recruitment of CD45+ (bone marrow derived cells), CD43+ (T-cells), and CD68+ (macrophages) cells, particularly in the adventitia. Hence, there is a need to consider both mechanobiological and immunobiological contributors to aortic wall growth (changes in mass) and remodeling (changes in microstructure). Although copious experimental data can provide insight into complex mechanisms of disease progression, well informed computational models can often provide further insight via parametric studies and numerical experiments. The goal of this paper, therefore, was to develop a computational model for progressive changes in aortic wall structure and function that occur in response to chronic AngII infusion in $Apoe^{-/-}$ mice with a specific focus on understanding better and contrasting the differential effects of immune cell recruitment and inflammation in the thoracic and abdominal aorta.

2. Methods

2.1. Experimental data

We recently reported experimental findings for 19-week old male $Apoe^{-/-}$ mice rendered hypertensive via a continuous infusion of AngII at $1000\,\mathrm{ng\,kg^{-1}\,min^{-1}}$ for up to 28 days (Bersi et al., 2017). Studying adult mice at this age and over a brief (four week) period obviates considerations of both somatic growth and vascular aging, thus allowing one to focus on hypertension-induced effects. Briefly, blood pressures were collected using a tail-cuff method, which revealed rapid increases up to 14 days, then little change thereafter. Specific values of systolic blood pressure were 111.6, 155.4, 167.6, 181.3, 183.9, and 186.2 mmHg after 0, 4, 7, 14, 21, and 28 days of infusion (diastolic, mean, and pulse pressures can similarly be found

in Supplemental Information in Bersi et al., 2017). Biaxial biomechanical data from seven different cyclic pressure-diameter and axial force-length protocols were collected after the same durations of AngII infusion (0, 4, 7, 14, 21, and 28 days) while immuno-histochemical data were collected after a subset of durations (0, 4, 14, and 28 days). By comparing changes in wall thickness with changes in blood pressure, we found that the IAA mechano-adapted at ≥ 14 days ($h \sim \gamma h_o$, with subscript o denoting the original homeostatic value and with $\varepsilon \sim 1$ due to unchanged cardiac output) while the DTA appeared to mechano-adapt by 14 days but then exhibited a marked maladaptation ($h \gg \gamma h_o$), resulting primarily from significant adventitial fibrosis. Long term follow-up (7 months after terminating the 28 days of AngII infusion) revealed further that this maladaptation persisted in the DTA despite removal of the exogenous inflammatory stimulus and a marked reduction in blood pressure to levels similar to non-infused age-matched controls.

2.2. Computational model

We recently presented a novel computational model of arterial growth and remodeling (G&R) that includes mechano- and immuno-stimulated matrix turnover and showed that this model can capture salient biomechanical features of the time-course of maladaptive remodeling of the thoracic aorta in WT mice infused with AngII at $490 \, \text{ng} \, \text{kg}^{-1} \, \text{min}^{-1}$ (Latorre and Humphrey, 2018b). Briefly, this constrained mixture model allows one to account for the evolution of aortic composition (i.e., mass fractions), mechanical properties, deposition stretches, and rates of turnover of multiple structurally significant constituents. Among the key equations are the mixture relation for biaxial wall stress,

$$\boldsymbol{\sigma}_\Gamma^\alpha(s) = \frac{1}{\rho} \int_{-\infty}^s m_\Gamma^\alpha(\tau) \, q_\Gamma^\alpha(s,\tau) \, \hat{\boldsymbol{\sigma}}_\Gamma^\alpha(s,\tau) \, d\tau \tag{1}$$

with

$$\hat{\boldsymbol{\sigma}}_\Gamma^\alpha(s,\tau) = \frac{2}{J_{\Gamma n(\tau)}^\alpha(s)} \mathbf{F}_{\Gamma n(\tau)}^\alpha(s) \frac{\partial \hat{W}^\alpha(\mathbf{C}_{\Gamma n(\tau)}^\alpha(s))}{\partial \mathbf{C}_{\Gamma n(\tau)}^\alpha(s)} \mathbf{F}_{\Gamma n(\tau)}^{\alpha T}(s) \tag{2}$$

where ρ is the wall mass density, $m_\Gamma^\alpha(\tau) > 0$ denotes the true rate of mass density production at G&R time τ, $q_\Gamma^\alpha(s,\tau) \in [0,1]$ is the fraction of material produced at time τ that survives to the current time $s \geq \tau$, and $\hat{W}^\alpha$ is the stored energy function; each term is constituent-

(α) and layer- ($\Gamma = M, A$ for media and adventitia, respectively) specific. $\mathbf{C}^\alpha_{\Gamma n(\tau)}(s) = \mathbf{F}^{\alpha T}_{\Gamma n(\tau)}(s)\,\mathbf{F}^\alpha_{\Gamma n(\tau)}(s)$ is the right Cauchy–Green tensor and $J^\alpha_{\Gamma n(\tau)}(s) = \det \mathbf{F}^\alpha_{\Gamma n(\tau)}(s)$ where

$$\mathbf{F}^\alpha_{\Gamma n(\tau)}(s) = \mathbf{F}_\Gamma(s)\,\mathbf{F}^{-1}_\Gamma(\tau)\,\mathbf{G}^\alpha_\Gamma(\tau) \tag{3}$$

is the constituent- and layer-specific deformation gradient, with $n(\tau)$ denoting potentially evolving constituent-specific natural (stress-free) configurations (consistent with a concept of adaptive homeostasis; Davies, 2016), $\mathbf{F}_\Gamma$ capturing mixture-level deformations (at time s or τ) relative to a common reference configuration, and $\mathbf{G}^\alpha_\Gamma(\tau)$ representing the "deposition stretch" at which the constituent is incorporated within each layer at a preferred prestress (Cyron and Humphrey, 2014). Moreover, we assume that mass density production and survival are governed constitutively by

$$m^\alpha_\Gamma(\tau) = k^\alpha_\Gamma(\tau)\,\rho^\alpha_\Gamma(\tau)\,\Upsilon^\alpha_\Gamma(\tau) \tag{4}$$

and

$$q^\alpha_\Gamma(s, \tau) = \exp\left(-\int_\tau^s k^\alpha_\Gamma(t)\,dt\right) \tag{5}$$

respectively, where $k^\alpha_\Gamma > 0$ is a rate parameter that governs constituent removal via a first-order type kinetic decay, ρ^α_Γ is the associated mass density, and $\Upsilon^\alpha_\Gamma > 0$ is a function that stimulates mass production at ($\Upsilon^\alpha_\Gamma = 1$), below ($\Upsilon^\alpha_\Gamma < 1$), or above ($\Upsilon^\alpha_\Gamma > 1$) basal levels. Whereas we previously modeled data for thoracic aortic maladaptation in WT mice infused with AngII at $490\,\mathrm{ng\,kg^{-1}\,min^{-1}}$ (Latorre and Humphrey, 2018b), preliminary simulations revealed that more complex constitutive relations were needed herein for $Apoe^{-/-}$ mice infused with AngII at $1000\,\mathrm{ng\,kg^{-1}\,min^{-1}}$. Consequently, we extended our prior model to include a rate parameter for constituent removal of the form

$$k^\alpha_\Gamma(t) = k^\alpha_{\Gamma 0}\left(1 + (\Delta\sigma(t))^2\right) \tag{6}$$

where $k_{\Gamma 0}^{\alpha}$ denotes a basal rate of removal. We similarly extended the immuno-mechano-stimulus function for constituent production to the form

$$\Upsilon_{\Gamma}^{\alpha}(\tau) = 1 + f_{\Gamma\sigma}^{\alpha}(\Delta\sigma(\tau)) - f_{\Gamma\tau}^{\alpha}(\Delta\tau_w(\tau)) + f_{\Gamma\varphi}^{\alpha}(\Delta\varrho_{\varphi}(\tau)) \tag{7}$$

where $\Delta\sigma$ and $\Delta\tau_w$ are deviations in pressure-induced intramural and flow-induced wall shear stress from homeostatic values, and $\Delta\varrho_{\varphi}$ is a measure of the evolving inflammatory cell burden (cf. Figure 3 in Bersi et al., 2017), with $f_{\Gamma\sigma}^{\alpha}$, $f_{\Gamma\tau}^{\alpha}$ and $f_{\Gamma\varphi}^{\alpha}$ generally nonlinear, monotonically increasing functions such that $f_{\Gamma\eta}^{\alpha}(0) = 0$ for $\eta = \sigma, \tau, \varphi$. Given the large stress differences $\Delta\sigma$ and $\Delta\tau_w$ reached in the DTA during the evolution of hypertensive remodeling, we defined sigmoidal (saturation) functions $f_{\Gamma\sigma}^{\alpha}(\Delta\sigma) = K_{\Gamma\sigma}^{\alpha}\arctan(\Delta\sigma)$ and $f_{\Gamma\tau}^{\alpha}(\Delta\tau_w) = K_{\Gamma\tau}^{\alpha}\arctan(\Delta\tau_w)$, whereas $f_{\Gamma\varphi}^{\alpha}(\Delta\varrho_{\varphi}) = K_{\Gamma\varphi}^{\alpha}\Delta\varrho_{\varphi}$ (as in Latorre and Humphrey, 2018b) consistent with the experimentally observed near linear correlation between morphological changes and inflammatory cell burden (see Figure 4 in Bersi et al., 2017). In addition, to describe the markedly maladaptive time-course data, we let the rate $k_{\Gamma 0}^{\alpha}$ and gain $K_{\Gamma\sigma}^{\alpha}$, $K_{\Gamma\tau}^{\alpha}$, $K_{\Gamma\varphi}^{\alpha}$ parameters evolve as a function of the inflammatory burden as

$$k_{\Gamma 0}^{\alpha}(\Delta\varrho_{\varphi}) = k_{\Gamma 0o}^{\alpha} + (k_{\Gamma 0h}^{\alpha} - k_{\Gamma 0o}^{\alpha})\, g_k(\Delta\varrho_{\varphi}) \tag{8}$$

and

$$K_{\Gamma\eta}^{\alpha}(\Delta\varrho_{\varphi}) = K_{\Gamma\eta o}^{\alpha} + (K_{\Gamma\eta h}^{\alpha} - K_{\Gamma\eta o}^{\alpha})g_K(\Delta\varrho_{\varphi}) \,, \quad \eta = \{\sigma, \tau, \varphi\} \tag{9}$$

where subscripts o and h denote original and evolved homeostatic values, with g_k and g_K generally nonlinear, monotonically increasing functions such that $g(0) = 0$ and $g(1) = 1$, for which sinusoidal functions $g_k(\Delta\varrho_{\varphi}) = g_K(\Delta\varrho_{\varphi}) = \sin(\frac{\pi}{2}\Delta\varrho_{\varphi})$ proved useful.

Finally, also following our prior study (Latorre and Humphrey, 2018b), we assumed that the intramural elastic fibers, smooth muscle, and collagen fibers could be described by the following stored energy functions:

$$\hat{W}^e(\mathbf{C}_{\Gamma}^e(s)) = \frac{c^e}{2}(\mathbf{C}_{\Gamma}^e(s) : \mathbf{I} - 3) \tag{10}$$

for an amorphous elastin-dominated matrix ($\alpha = e$), where c^e is a shear modulus, and

$$\hat{W}^\alpha(\lambda_{n(\tau)}^\alpha(s)) = \frac{c_1^\alpha}{4c_2^\alpha}\left[e^{c_2^\alpha((\lambda_{n(\tau)}^\alpha(s))^2-1)^2} - 1\right] \tag{11}$$

for a circumferentially oriented composite of collagen fiber and passive smooth muscle ($\alpha = m$) plus axially and diagonally oriented collagen fibers ($\alpha = c$) in the media as well as circumferentially, axially, and diagonally oriented collagen fibers in the adventitia, with c_1^α and c_2^α material parameters and $\lambda_{n(\tau)}^\alpha(s)$ the corresponding stretch. Note that these functions together constitute a layer-specific "four-fiber family" model, with effects of other constituents (such as proteoglycans) captured phenomenologically via a fit to data. Additional details regarding the G&R model development and implementation can be found elsewhere (Latorre and Humphrey, 2018b).

2.3. Parameter estimation

Whereas some of the key model parameters can be determined directly from experimentally measured data (e.g., initial wall geometry, mass fractions, and in vivo state of stress and strain), we have developed a systematic, step-by-step, nonlinear regression approach to determine many of the other parameters from available histological and biaxial mechanical data. Such regression yields best-fit values of constituent-specific material parameters and deposition stretches (cf. Appendix in Latorre and Humphrey, 2018b). Note, too, that we used the unloading curves from the biaxial data to capture only that part of the energy that was stored during loading and was subsequently available to do work. Importantly, energy dissipation (hysteresis) is generally small over loads imposed during a cardiac cycle. Finally, because some of the requisite parameter values cannot be determined from nonlinear regressions, we also developed (in that same Appendix) a method for estimating values of the gain-type parameters for constituent production and rate parameters for constituent removal, which herein include an additional dependence on inflammatory cell burden (Eqs. (8) and (9)). Importantly, experimental data collected at different times over the course of AngII infusion (0, 4, 7, 14, 21, and 28 days) allows one to estimate parameters that evolve with the extent of inflammatory burden. By assuming an immunomechanobiologically equilibrated evolution, we apply the aforementioned nonlinear regression method particularized

7

at intermediate times to estimate how model parameters evolve over the four-week period of AngII infusion.

3. Results

Table 1 lists values of the model parameters for the locally mechano-adapted IAA and maladapted DTA based on experimental results reported in Bersi et al. (2017); it was further assumed that both segments maintained the same overall mass density $\rho = 1050\,\mathrm{kg\,/\,m^3}$. For some parameters we list both original (homeostatic, at day 0) and final (perhaps homeostatic, at day 28) values, again assuming a potentially adaptive homeostasis thus allowing "short-term adaptations to set-points, and to the range of 'normal' capacity" (Davies, 2016). For example, best-fit tensile collagen parameters evolved from $[c_1^{c+}, c_2^{c+}] = [450\,\mathrm{kPa}, 3.51]$ to $[309\,\mathrm{kPa}, 4.62]$ for the IAA over the four weeks of AngII induced hypertension. In contrast, these same parameters evolved more dramatically for the DTA, from $[297\,\mathrm{kPa}, 5.36]$ to $[393\,\mathrm{kPa}, 38.5]$, suggestive of a marked matrix remodeling beyond simply replacing prior constituents with new constituents having only a different natural configuration. Figure 1 shows both representative fits of the model to pressure-diameter and axial force-stretch data as well as predicted time course of changes in both the collagen and smooth muscle parameters for the IAA and DTA, computed as functions of the inflammatory cell density. To reduce the number of parameters to be determined from intermediate nonlinear regressions, the deposition stretches and parameters in compression (not shown) were prescribed to evolve linearly, at most, between respective original $(\Delta\varrho_\varphi = 0)$ and final $(\Delta\varrho_\varphi = 1)$ values. Again, the time course of changes were less marked in the IAA than in the DTA. For example, the deposition stretch for collagen G^c remained near 1.20 for the IAA but evolved from 1.20 to 1.05 for the DTA. Amongst the many other parameters, the gains associated with collagen production similarly changed (increased) much more for the DTA than the IAA, especially in the adventitia, while the rate parameters driving degradation changed modestly for both the IAA and DTA. Taken together, these results reflect the experimental findings that G&R was more dramatic in the DTA than the IAA and especially so in the adventitia.

Our model-based results suggest further, however, that this G&R could be heightened considerably by an inflammation-mediated increase in the rate of production of collagen

having different properties. Given that one must be careful not to over-interpret parameter values in nonlinear models, it is prudent to focus more on the predicted tissue-level consequences. Hence, note that the resulting parameterized model allows one to simulate the evolution of multiple geometric and mechanical metrics, including wall thickness (h), the preferred in vivo axial stretch (λ_z^{iv}), biaxial wall stress ($\sigma_{\theta\theta}$, σ_{zz}) and material stiffness ($c_{\theta\theta\theta\theta}$, c_{zzzz}), elastically stored energy (W), and overall distensibility ($\mathcal{D}$), all of which were computed with our full heredity integral-based model. Moreover, at any time during a simulation, we can perform a "numerical biaxial test" to plot structural (pressure-diameter and axial force-length) and material (Cauchy stress-stretch) responses. For example, Figure 2 shows predicted structural and material responses for the IAA and DTA at 0, 7, 14, 21, and 28 days of AngII-induced hypertension, with either no inflammation (i.e., assumed mechano-stimulated G&R alone, due primarily to pressure elevation) or inflammation prescribed based on experimental findings (cf. Figure 3 in Bersi et al. (2017)). When including the effects of inflammation, pressure-diameter responses tend to evolve toward a stiffer response, especially in the DTA. More dramatically, the axial force-stretch results show a progressive left-ward shift in both cases and aortic regions, indicative largely of an evolving reduction in the preferred value of the axial stretch. Finally, the predicted biaxial mechanical properties show modest left-ward shifts, more dramatic in the DTA, wherein an overall reduction in wall stress is seen at comparable distending pressures, suggestive largely of the evolving increase in wall thickness.

Indeed, Figure 3 shows model inputs (i.e., prescribed time courses for the blood pressure elevation as well as inflammatory burden in the IAA and DTA) and associated experimentally measured (symbols) and computationally predicted (lines) changes in luminal radius and wall thickness, with the latter delineated for the media and adventitia. As it can be seen, the model captured the measured findings well for the IAA when either excluding or including the observed modest level of inflammation; it similarly captured well the measurements for the DTA up to 14 days whether excluding or including the inflammation, but results from 14 to 28 days for the DTA could be captured only when including inflammation. These findings – that inflammation played little role in the IAA while it played a dramatic role in the DTA after two weeks – are consistent with that observed by Bersi et al.

9

(2017), but we emphasize here that we first attempted to fit all of the data without inflammation or evolving properties and only then extended the model as appropriate to capture the actual experimental observations. Toward this end, note that the near preservation of the lumen in the IAA likely maintained wall shear stress near normal while the inward remodeling in the DTA likely increased wall shear stresses. One would expect increased wall shear stresses to increase nitric oxide production by the endothelium and hence vasodilatation, but it appears that this normal response mechanism was compromised (i.e., that there was endothelial dysfunction, but this was not assessed experimentally). Finally, Figure 4 shows the effect of measured inflammation on the predicted evolution of eight additional geometrical or mechanical metrics in the IAA and DTA. Again many metrics change more dramatically in the DTA, particularly in the presence of inflammation after 14 days. Total wall thickness increases and the preferred in vivo axial stretch decreases, which together tend to reduce the early hypertension-induced increase in biaxial wall stresses; these stresses tend toward baseline values in the IAA but to values much lower than baseline in the DTA due to the exuberant inflammation-driven thickening after 14 days. Interestingly, the circumferential material stiffness is maintained near normal in both segments while the axial stiffness decreases from baseline in the DTA alone. Computed distensibility $\mathcal{D}$ decreases in both segments with time of AngII infusion, again more dramatically in the DTA.

Figure 5 shows model predictions for the long-term evolution, over 224 days, of inner radius and wall thickness in the DTA given either a vanishing inflammatory cell burden or merely a decrease in inflammation following cessation of AngII infusion at 28 days and a return of blood pressure toward normal. Importantly, just as the model was only able to capture the 28 day responses in the DTA by including significant inflammation (Figures 1, 3, and 4), it was only able to capture the long-term responses by including a lower, but persistent inflammation. This finding motivated us to re-evaluate previously unpublished data at the 224 day endpoint (cf. Bersi et al., 2017). As it can be seen in the bottom panels of Figure 5, these data confirmed the model predictions of a persistent level of inflammation.

Finally, we have recently shown in a similar (simplified) computational model for arterial G&R that low values of the parameters governing the rate of matrix synthesis (e.g., gain parameters $K_{\Gamma\eta}^{\alpha}$ in Eq. (9)), or low ratios of in vivo stiffness to (pre)stress (e.g., $c_{\theta\theta\theta\theta o}/2\sigma_{\theta\theta o}$),

10

can both result in uncontrolled dilation and thickening over G&R time scales following transient perturbations in blood pressure (Latorre and Humphrey, 2019). Therefore, even though the present modeling is more complex (with a bilayered, rather than unilayered, wall; nonlinear, rather than linear, stimulus functions for mass production, including inflammatory effects; and inflammation-dependent, rather than constant, properties), it is worthwhile to investigate roles of these properties in the present case from a perspective of mechanobiological stability. In fact, (stable) plateaus for geometric, material, and structural properties were observed after 14 days of AngII infusion in both experiments (Bersi et al., 2016) and subsequent modeling (Latorre and Humphrey, 2018b) for WT mice subject to a lower rate of AngII infusion. In contrast, because evolved plateaus were not experimentally apparent in the present case, especially for the DTA (Figures 3 and 4), and perhaps because of the higher rate of AngII infusion or different mouse model, results from our computations can yield insight into possible mechanobiological stability properties of evolved (mal)adaptive states. Albeit not shown, the model, with parameters in Table 1 and inputs (inner pressure and inflammation burden) sustained as $P(s > 28)/P_o = P(s = 28)/P_o = 1.68$ and $\Delta\varrho_\varphi(s > 28) = \Delta\varrho_\varphi(s = 28) = 1$, predicted asymptotically stable evolutions towards respective evolved states in both regions (adaptive for the IAA, maladaptive for the DTA), hence consistent with the aforementioned stabilizations observed in WT mice, although delayed. Similar stable responses under transient perturbations in pressure were obtained at $s = 224$ days for the DTA at the respective evolved state (Figure 5). Furthermore, consideration of 50% lower values of either gain parameters (all reduced proportionally) or stiffness components for medial smooth muscle cells and adventitial collagen (while preserving associated stresses) still yielded asymptotically stable responses towards the same evolved states, although with oscillations of higher amplitude, consistent with results in Latorre and Humphrey (2019). Considered together, these results suggest further that the fibrotic response observed mainly in the DTA, while being maladaptive and hence compromising homeostasis, seems to preserve mechanobiological stability, which suggests that it may be challenging to reverse maladaptive remodeling once entrenched.

4. Discussion

One can define a local mechano-adaptation of the aorta as cell-mediated changes in geometry and wall composition that either maintain or restore toward normal both the pressure-induced mean circumferential wall stress ($\sigma_{\theta\theta} = Pa/h$) and the flow-induced mean wall shear stress ($\tau_w = 4\mu Q/\pi a^3$), with P denoting the distending pressure, Q the volumetric flow rate, a the inner radius, h the wall thickness, and μ the viscosity of the blood. We previously showed experimentally that, according to this definition, a 28-day moderate rate of infusion of AngII in male C57BL/6 mice leads to grossly maladaptive G&R of the DTA (Bersi et al., 2016), and that a descriptive computational model can capture such observations by including inflammation as well as the usual mechano-stimulation of matrix turnover (Latorre and Humphrey, 2018b). We similarly found experimentally that a 28-day high rate of infusion of AngII in male $Apoe^{-/-}$ mice on a C57BL/6 background results in a gross maladaptation of the DTA, which persisted for at least 7 months after ending the AngII infusion; in stark contrast there is a near perfect mechano-adaptation of the IAA (Bersi et al., 2017). Figures 2 to 5 demonstrate that our mechano-driven, immuno-mediated computational model of aortic G&R is able to delineate the differential hypertension-induced evolutions of geometry and material properties in the DTA and IAA, the former with a significantly higher inflammatory burden that was predicted to persist, in part, following cessation of AngII infusion after 28 days. Indeed, a subsequent re-evaluation of experimental data confirmed this prediction. Importantly, capturing these experimental findings with our model required that the material parameters for collagen / passive smooth muscle evolve and so too the gain- and rate-parameters for extracellular matrix production and removal (Table 1). The former appears to be consistent with measured differences in collagen fiber diameter in the common carotid artery from an aortic coarctation model of induced hypertension (Eberth et al., 2009) and in the DTA in an AngII model of induced hypertension (Korneva and Humphrey, 2019), both in the mouse; the latter in turn appears to be qualitatively consistent with measurements of increased turnover rates in a model of hypertension in rats (Nissen et al., 1978). Note that inducing hypertension via coarctation of the aortic arch in the mouse also results in marked fibrosis of the thoracic aorta within a short period (14 days) that is also driven by inflammation, as evidenced by increases in IL-6 and monocyte chemoattrant protein-1

(MCP-1) that appear to be mediated by AngII since the associated remodeling is attenuated by Losartan, a specific type 1 AngII receptor antagonist (Kuang et al., 2013). We would thus expect that salient features from our modeling of mechano- and immuno-mediated G&R in the aorta would also hold for other forms of induced hypertension.

It is important to note that although some material parameters had to evolve in our current G&R model, our current quantitative modeling of evolution is very different from that which was reported previously (Eberth et al., 2011), wherein different sets of best-fit parameters were determined via nonlinear regression for the same hyperelastic constitutive relation at different times of aortic coarctation-induced hypertension. Indeed, fitting different data sets with separate sets of material parameters has been common in modeling the effects of hypertension (Hayashi and Naiki, 2009) and aortic aging (Ferruzzi et al., 2011; Waffenschmidt et al., 2016). In contrast, we used a constrained mixture model of G&R to describe and predict the evolving vascular geometry and properties based primarily on validated relations for rates of mass production and removal (Valentín and Humphrey, 2009), with production now depending directly on both mechanical stimuli and inflammatory cell burden (Eqs. (4) and (7)). Prior models of arterial G&R in hypertension (e.g., Tsamis et al., 2009; Rachev and Gleason, 2011) have not included effects of inflammation directly, but here we suggest that both mechano-driven and immuno-mediated matrix turnover are critical in hypertensive vascular remodeling and (mal)adaptation; such inclusion alone has allowed us to model the regional differences within the aorta considered herein. Importantly, the present model not only emphasizes the centrality of the extent and time-course of the inflammatory burden (Figure 3), it also highlights the importance of altered rates of matrix turnover, with fibrosis resulting from marked increases in deposition in the absence of corresponding increases in degradation. The search for potentially improved therapeutics should thus seek to reduce the pressure elevation and inflammatory burden without compromising appropriate proteolytic activity.

AngII has been reported to increase significantly the pulse wave velocity and material stiffness of the thoracic and abdominal aorta in $Apoe^{-/-}$ mice (Tham et al., 2002). The latter was measured using ring tests, however, which do not capture the complexities of biaxial G&R. Indeed, our experimental findings show that the circumferential material stiffness is

maintained near original values in both WT and $Apoe^{-/-}$ mice subject to AngII-induced hypertension (Bersi et al., 2016, 2017), which suggests that the intramural cells retain an ability to mechano-sense and -regulate the extracellular matrix (Bellini et al., 2017; Humphrey et al., 2015). Biaxial tests have also been employed by others to study the thoracic and abdominal aorta of $Apoe^{-/-}$ mice as a function of age and diet (Agianniotis and Stergiopulos, 2012; Cilla et al., 2016), but not as a function of AngII-induced hypertension and inflammation; it was for this reason that we focused on describing our prior biaxial data (Bersi et al., 2017). As seen in Figure 4, our G&R model captures these biaxial data sets well. Importantly, the combination of a marked thickening of the aortic wall—adaptively in the IAA and excessively in the DTA—with preserved circumferential material stiffness would nevertheless increase the structural stiffness in vivo, which in turn would be expected to increase the pulse wave velocity as observed experimentally (Hartley et al., 2000; Tham et al., 2002). Whereas pulse wave velocity is an integrated (global) measure of vascular health, our findings delineate the potential local biomechanical mechanisms for this increase in structural stiffening and the regional differences therein.

Notwithstanding the ability of the present and past models to describe and predict diverse G&R responses in the vasculature, there is a pressing need for continued model advancement. For example, although one can use evolving values of diastolic, mean, or systolic pressures to drive G&R in hypertension models (herein we used systolic given the prior observation of a statistically significant correlation between aortic changes and systolic, but not mean, arterial pressure; Eberth et al., 2009), the intramural cells appear to respond most to changes in pulse pressure (Lacolley et al., 2009; Scott et al., 2012), that is, cyclic changes in wall stress or strain. This can be accounted for by positing and testing stimulus functions that account for changes in cyclic loading (cf. Cardamone et al., 2010), particularly since local pulse pressures often differ from region to region within the aorta (Cuomo et al., 2019). More experimental data will be needed to investigate this important aspect of the mechanobiology, however.

There is also a need to understand better what drives regional differences in inflammation and to model the molecular drivers rather than simply to prescribe phenomenologically the measured inflammatory cell burden, particularly since cytokine profiles differ by sex even

14

for the same cell type (Ji et al., 2014). We included inflammatory cell density – based on total local bone marrow derived (CD45+) cell expression – directly in the production term because proinflammatory cytokines, such as the T-cell associated IL-17a, increase collagen gene expression in synthetic cells and contribute to hypertensive remodeling (Wu et al., 2014). We also assumed that matrix removal depended on a stress stimulus since increased mechanical loading increases both MMP activity (Asanuma et al., 2003) and the resistance of matrix to degradation (Ruberti and Hallab, 2005). More data are needed to better understand and model these opposing actions in response to the same stimulus. Unlike our modeling of the WT aortic maladaptation (Latorre and Humphrey, 2018b), evolving rate parameters for matrix removal were also needed to predict the time-course data available, seemingly consistent with prior experiments in other rodent models (Nissen et al., 1978). This important emergent finding also appears to be consistent with the notion that inflammation contributes to homeostasis, but its prioritization (to otherwise protect against threats) allows it to over-ride or suppress other homeostatic mechanisms, often resulting in changes in set-points and entrenching alternative stable states (Kotas and Medzhitov, 2015). Our prior data also suggest that inflammatory cell infiltration followed, and thus may have been stimulated by, the pressure-induced increase in wall stress (Bersi et al., 2017), hence supporting our phenomenological modeling assumptions. Nevertheless, inflammation should be considered more precisely and explicitly in both the production and removal equations when more quantitative data become available. In particular, inflammation involves cells from diverse hematopoeitic lineages—such as myeloid (e.g., monocytes, macrophages, and dendritic cells) and lymphoid (e.g., T-cells and B-cells)—which secrete myriad chemokines (MCP-1), cytokines (IL-6, IL-17a, TNF, and so forth), and proteases (MMP-2,9,13, among others) that impact extracellular matrix remodeling; thus there is a need for cellular- and molecular-specific models to be incorporated within a G&R model. Only in this way will we be able to simulate potential pharmacotherapies and immunotherapeutic treatment strategies.

Indeed, more mechanistic models should also account for regional differences in cell phenotype, including receptor distributions. Although the DTA and IAA include smooth muscle cells derived from similar embryonic lineages (somatic and splanchnic mesoderm; Majesky,

2007), there is yet a considerable increase from the proximal to distal aorta in type 1 AngII receptor (AT1aR and At1bR) density (Poduri et al., 2012) and associated contractile responses to AngII (Rateri et al., 2011). Alternatively, expression of connexins (Cx43 and Cx45) decreases from the proximal to distal aorta (Ko et al., 2001), noting that connexins play roles in aortic contractility and they change expression in AngII-induced hypertension (Alonso et al., 2010). We recently found that increased adventitial fibrosis tends to correlate with a progressive loss in smooth muscle contractility in the DTA (Korneva and Humphrey, 2019), hence emphasizing the need for greater attention to the roles of endothelial and smooth muscle function. These, and other, regional differences could play important roles beyond just differences in local pulse pressure and inflammatory cell burden in driving differential G&R along the aorta and should eventually be modeled.

Finally, we used a full heredity integral based constrained mixture model since different constituents can be incorporated within extant matrix at different times relative to constituent-specific natural configurations, yet such modeling can be computationally expensive. There is, therefore, motivation to seek simpler constrained mixture models. We have show that some simplifications can be achieved depending on the differential rates of mechanical loading and matrix turnover (Latorre and Humphrey, 2018a), which may be exploited in cases wherein pressure loading and inflammatory burden exhibit different time-courses. Further experimental attention to the rates of change in mechanical loading, infiltration and activation of inflammatory cells, and cell/matrix turnover could allow for both more precise modeling and computationally less expensive simulations. In this work, a simplified framework allowed us to parameterize our mathematical model by means of nonlinear regressions of experimental data as a first approximation to the actual evolution.

In conclusion, we have presented a new computational model of G&R that delineates local mechano-adaptive and maladaptive growth and remodeling as a function of aortic region in AngII-induced hypertension, which required explicit consideration of consequences of regional differences in inflammatory cell burden. That is, a purely mechano-mediated G&R model was not able to capture measured geometrical or mechanical changes in the DTA after 14 days of infusion, when inflammation manifested most dramatically. Our simulations suggested further that such inflammation persists for long periods after removing

the exogenous (AngII) stimulus, and new experimental data presented herein supports this prediction. It could be that fibrotic matrix produced during AngII infusion could differ slightly in composition or turnover more slowly, thereby stimulating preserved or additional deposition of matrix with altered properties (cf. Parker et al., 2014). There is clearly a need for additional experimental investigation of this key issue, which may contribute to the clinical observation that pharmacological treatment of hypertension must continue, once started, which is to say it has yet been impossible to reverse. Whereas mechanical homeostasis is promoted by negative feedback loops, as captured by the stress-difference term in our stimulus function, fibrosis appears to be driven either by positive feedback or no feedback, as modeled presently. Understanding such feedback loops, and the associated (in)stabilities (Schwartz et al., 2018), also promises to provide increased insight into possible treatment strategies. Toward this end, there is also a pressing need to understand better the possible role of inflammation in altering or over-riding mechanical homeostasis, perhaps via persistent changes in set-points (Kotas and Medzhitov, 2015). Finally, we focused on local mechano-adaptation or maladaptation. There is a need to explore better the coupled effects between local mechanics and global hemodynamics, noting that local adaptations can be beneficial at the cell-tissue level and yet detrimental to the global circulatory system, thus establishing broader feedback loops that can ultimately drive disease (Humphrey et al., 2016; Laurent and Boutouyrie, 2015). Much thus remains to be understood, and we submit that computational G&R models promise to aid considerably in this pursuit.

References

Agianniotis A, Stergiopulos N (2012) Wall properties of the apolipoprotein E-deficient mouse aorta. Atherosclerosis 223(2):314–320

Alonso F, Krattinger N, Mazzolai L, Simon A, Waeber G, Meda P, Haefliger JA (2010) An angiotensin II- and NF-κB-dependent mechanism increases connexin 43 in murine arteries targeted by renin-dependent hypertension. Cardiovascular research 87(1):166–176

Asanuma K, Magid R, Johnson C, Nerem RM, Galis ZS (2003) Uniaxial strain upregulates matrix-degrading enzymes produced by human vascular smooth muscle cells. American Journal of Physiology-Heart and Circulatory Physiology 284(5):H1778–H1784

Bardy N, Merval R, Benessiano J, Samuel JL, Tedgui A (1996) Pressure and angiotensin II synergistically induce aortic fibronectin expression in organ culture model of rabbit aorta: evidence for a pressure-induced tissue renin-angiotensin system. Circulation Research 79(1):70–78

Bellini C, Bersi MR, Caulk AW, Ferruzzi J, Milewicz DM, Ramirez F, Rifkin DB, Tellides G, Yanagisawa H, Humphrey JD (2017) Comparison of 10 murine models reveals a distinct biomechanical phenotype in thoracic aortic aneurysms. Journal of The Royal Society Interface 14(130):20161036

Bersi MR, Bellini C, Wu J, Montaniel KRC, Harrison DG, Humphrey JD (2016) Excessive adventitial remodeling leads to early aortic maladaptation in angiotensin-induced hypertension. Hypertension 67:890–896

Bersi MR, Khosravi R, Wujciak AJ, Harrison DG, Humphrey JD (2017) Differential cell-matrix mechanoadaptations and inflammation drive regional propensities to aortic fibrosis, aneurysm or dissection in hypertension. Journal of The Royal Society Interface 14(136):20170327

Cardamone L, Valentin A, Eberth JF, Humphrey JD (2010) Modelling carotid artery adaptations to dynamic alterations in pressure and flow over the cardiac cycle. Mathematical medicine and biology 27(4):343–371

Cilla M, Perez MM, Pena E, Martinez MA (2016) Effect of diet and age on arterial stiffening due to atherosclerosis in ApoE$^{-/-}$ mice. Annals of biomedical engineering 44(7):2202–2217

Cuomo F, Ferruzzi J, Agarwal P, Li C, Zhuang ZW, Humphrey JD, Figueroa CA (2019) Sex-dependent differences in central artery haemodynamics in normal and fibulin-5 deficient mice: implications for ageing. Proceedings of the Royal Society A 475(2221):20180076

Cyron CJ, Humphrey JD (2014) Vascular homeostasis and the concept of mechanobiological stability. International journal of engineering science 85:203–223

Davies KJA (2016) Adaptive homeostasis. Molecular aspects of medicine 49:1–7

Eberth JF, Gresham VC, Reddy AK, Popovic N, Wilson E, Humphrey JD (2009) Importance of pulsatility in hypertensive carotid artery growth and remodeling. Journal of hypertension 27(10):2010

Eberth JF, Cardamone L, Humphrey JD (2011) Evolving biaxial mechanical properties of mouse carotid arteries in hypertension. Journal of biomechanics 44(14):2532–2537

Ferruzzi J, Vorp DA, Humphrey JD (2011) On constitutive descriptors of the biaxial mechanical behaviour of human abdominal aorta and aneurysms. Journal of The Royal Society Interface 8(56):435–450

Hartley CJ, Reddy AK, Madala S, Martin-McNulty B, Vergona R, Sullivan ME, Halks-Miller M, Taffet GE, Michael LH, Entman ML, Wang YX (2000) Hemodynamic changes in apolipoprotein E-knockout mice. American Journal of Physiology-Heart and Circulatory Physiology 279(5):H2326–H2334

Hayashi K, Naiki T (2009) Adaptation and remodeling of vascular wall; biomechanical response to hypertension. Journal of the Mechanical Behavior of Biomedical Materials 2(1):3–19

Humphrey JD (2008) Mechanisms of arterial remodeling in hypertension. Hypertension 52(2):195–200

Humphrey JD, Schwartz MA, Tellides G, Milewicz DM (2015) Role of mechanotransduction in vascular biology: focus on thoracic aortic aneurysms and dissections. Circulation research 116(8):1448–1461

Humphrey JD, Harrison DG, Figueroa CA, Lacolley P, Laurent S (2016) Central artery stiffness in hypertension and aging: a problem with cause and consequence. Circulation research 118(3):379–381

Ji H, Zheng W, Li X, Liu J, Wu X, Zhang MA, Umans JG, Hay M, Speth RC, Dunn SE, Sandberg K (2014) Sex-specific T-cell regulation of angiotensin II–dependent hypertension. Hypertension 64(3):573–582

Ko YS, Coppen SR, Dupont E, Rothery S, Severs NJ (2001) Regional differentiation of desmin, connexin43, and connexin45 expression patterns in rat aortic smooth muscle. Arteriosclerosis, thrombosis, and vascular biology 21(3):355–364

Korneva A, Humphrey JD (2019) Maladaptive aortic remodeling in hypertension associates with dysfunctional smooth muscle contractility. American Journal of Physiology-Heart and Circulatory Physiology 316(2):H265–H278

Kotas ME, Medzhitov R (2015) Homeostasis, inflammation, and disease susceptibility. Cell 160(5):816–827

Kuang SQ, Geng L, Prakash SK, Cao JM, Guo S, Villamizar C, Kwartler CS, Peters AM, Brasier AR, Milewicz DM (2013) Aortic remodeling after transverse aortic constriction in mice is attenuated with AT1 receptor blockade. Arteriosclerosis, thrombosis, and vascular biology 33(9):2172–2179

Lacolley P, Safar ME, Regnault V, Frohlich ED (2009) Angiotensin II, mechanotransduction, and pulsatile arterial hemodynamics in hypertension. American Journal of Physiology-Heart and Circulatory Physiology 297(5):H1567–H1575

Latorre M, Humphrey JD (2018a) Critical roles of time-scales in soft tissue growth and remodeling. APL Bioengineering 2(2):026108

Latorre M, Humphrey JD (2018b) Modeling mechano-driven and immuno-mediated aortic maladaptation in hypertension. Biomechanics and Modeling in Mechanobiology 17(5):1497–1511

Latorre M, Humphrey JD (2019) Mechanobiological stability of biological soft tissues. Journal of the Mechanics and Physics of Solids 125:298–325

Laurent S, Boutouyrie P (2015) The structural factor of hypertension: large and small artery alterations. Circulation research 116(6):1007–1021

Li Q, Muragaki Y, Hatamura I, Ueno H, Ooshima A (1998) Stretch-induced collagen synthesis in cultured smooth muscle cells from rabbit aortic media and a possible involvement of angiotensin II and transforming growth factor-β. Journal of vascular research 35(2):93–103

Louis H, Kakou A, Regnault V, Labat C, Bressenot A, Gao-Li J, Gardner H, Thornton SN, Challande P, Li Z, Lacolley P (2007) Role of $\alpha 1\beta 1$-integrin in arterial stiffness and angiotensin-induced arterial wall hypertrophy in mice. American Journal of Physiology-Heart and Circulatory Physiology 293(4):H2597–H2604

Majesky MW (2007) Developmental basis of vascular smooth muscle diversity. Arteriosclerosis, thrombosis, and vascular biology 27(6):1248–1258

Nissen R, Cardinale GJ, Udenfriend S (1978) Increased turnover of arterial collagen in hypertensive rats. Proceedings of the National Academy of Sciences 75(1):451–453

Parker MW, Rossi D, Peterson M, Smith K, Sikström K, White ES, Connett JE, Henke CA, Larsson O, Bitterman PB (2014) Fibrotic extracellular matrix activates a profibrotic positive feedback loop. The Journal of clinical investigation 124(4):1622–1635

Poduri A, Owens III AP, Howatt DA, Moorleghen JJ, Balakrishnan A, Cassis LA, Daugherty A (2012) Regional variation in aortic AT1b receptor mRNA abundance is associated with contractility but unrelated to atherosclerosis and aortic aneurysms. PLoS One 7(10):e48462

Rachev A, Gleason RL (2011) Theoretical study on the effects of pressure-induced remodeling on geometry and mechanical non-homogeneity of conduit arteries. Biomechanics and Modeling in Mechanobiology 10(1):79–93

Rateri DL, Moorleghen JJ, Balakrishnan A, Owens III AP, Howatt DA, Subramanian V, Poduri A, Charnigo R, Cassis LA, Daugherty A (2011) Endothelial cell–specific deficiency of Ang II type 1a receptors attenuates Ang II–induced ascending aortic aneurysms in LDL receptor$^{-/-}$ mice. Circulation research 108(5):574–581

Ruberti JW, Hallab NJ (2005) Strain-controlled enzymatic cleavage of collagen in loaded matrix. Biochemical and biophysical research communications 336(2):483–489

Schwartz MA, Vestweber D, Simons M (2018) A unifying concept in vascular health and disease. Science 360(6386):270–271

Scott D, Tan Y, Shandas R, Stenmark KR, Tan W (2012) High pulsatility flow stimulates smooth muscle cell hypertrophy and contractile protein expression. American Journal of Physiology-Lung Cellular and Molecular Physiology 304(1):L70–L81

Tham DM, Martin-McNulty B, Wang YX, Da Cunha V, Wilson DW, Athanassious CN, Powers AF, Sullivan ME, Rutledge JC (2002) Angiotensin II injures the arterial wall causing increased aortic stiffening in apolipoprotein E-deficient mice. American Journal of Physiology-Regulatory, Integrative and Comparative Physiology 283(6):R1442–R1449

Tieu BC, Lee C, Sun H, LeJeune W, Recinos A, Ju X, Spratt H, Guo DC, Milewicz D, Tilton RG, Brasier AR (2009) An adventitial IL-6/MCP1 amplification loop accelerates macrophage-mediated vascular inflammation leading to aortic dissection in mice. The Journal of clinical investigation 119(12):3637–3651

Tsamis A, Stergiopulos N, Rachev A (2009) A structure-based model of arterial remodeling in response to sustained hypertension. Journal of Biomechanical Engineering 131(10):101004

Valentín A, Humphrey JD (2009) Evaluation of fundamental hypotheses underlying constrained mixture models of arterial growth and remodelling. Philosophical Transactions of the Royal Society of London A: Mathematical, Physical and Engineering Sciences 367(1902):3585–3606

Waffenschmidt T, Cilla M, Sáez P, Pérez MM, Martínez MA, Menzel A, Peña E (2016)

Towards the modelling of ageing and atherosclerosis effects in ApoE$^{-/-}$ mice aortic tissue. Journal of biomechanics 49(12):2390–2397

Wu J, Thabet SR, Kirabo A, Trott DW, Saleh MA, Xiao L, Madhur MS, Chen W, Harrison DG (2014) Inflammation and mechanical stretch promote aortic stiffening in hypertension through activation of p38 mitogen-activated protein kinase. Circulation Research 114:616–625

Prescribed data		IAA	DTA
Inner Radius, Thickness (sys, o)	a_o, h_{Mo}, h_{Ao}	$[417, 17, 15]\mu m$	$[710, 29, 13]\mu m$
Inner Radius, Thickness (sys, h)	a_h, h_{Mh}, h_{Ah}	$[464, 30, 23]\mu m$	$[514, 48, 114]\mu m$
Medial Mass Fraction (o)	$\phi_{Mo}^e, \phi_{Mo}^m, \phi_{Mo}^c$	0.154, 0.651, 0.195	0.344, 0.461, 0.195
Medial Mass Fraction (h)	$\phi_{Mh}^e, \phi_{Mh}^m, \phi_{Mh}^c$	0.076, 0.690, 0.234	0.300, 0.500, 0.200
Adventitial Mass Fraction (o)	$\phi_{Ao}^e, \phi_{Ao}^m, \phi_{Ao}^c$	0.003, 0.0, 0.997	0.017, 0.0, 0.983
Adventitial Mass Fraction (h)	$\phi_{Ah}^e, \phi_{Ah}^m, \phi_{Ah}^c$	0.002, 0.0, 0.998	0.002, 0.0, 0.998
In vivo Axial Stretch (o, h)	$\lambda_{zo}^{iv}, \lambda_{zh}^{iv}$	1.81, 1.63	1.55, 1.32
Progressive best-fit to end-point data		IAA	DTA
Diagonal Collagen Orientation	α_0	30.7°	32.1°
Layer-specific Collagen Fractions	$\beta_A^\theta, \beta_M^z = \beta_A^z$	0.058, 0.057	0.044, 0.057
Elastin Parameter	c^e	114kPa	92.4kPa
Elastin Deposition Stretches	G_r^e, G_θ^e, G_z^e	$1/G_\theta^e G_z^e$, 1.96, 1.73	$1/G_\theta^e G_z^e$, 1.92, 1.72
Muscle Param: Tens / Comp (o)	$c_{1o}^{m+}, c_{2o}^{m+}, c_{1o}^{m-}, c_{2o}^{m-}$	343kPa, 1.23, 129kPa, 0.05	497kPa, 0.27, 198kPa, 0.03
Muscle Param: Tens / Comp (h)	$c_{1h}^{m+}, c_{2h}^{m+}, c_{1h}^{m-}, c_{2h}^{m-}$	440kPa, 0.08, 6.56kPa, 0.08	310kPa, 3.15, 0.97kPa, 0.71
Collagen Param: Tens / Comp (o)	$c_{1o}^{c+}, c_{2o}^{c+}, c_{1o}^{c-}, c_{2o}^{c-}$	450kPa, 3.51, 2.13kPa, 0.08	297kPa, 5.36, 143kPa, 0.07
Collagen Param: Tens / Comp (h)	$c_{1h}^{c+}, c_{2h}^{c+}, c_{1h}^{c-}, c_{2h}^{c-}$	309kPa, 4.62, 16.6kPa, 4.62	393kPa, 38.5, 0.98kPa, 27.9
Deposition Stretches (o)	G_o^m, G_o^c	1.17, 1.20	1.19, 1.20
Deposition Stretches (h)	G_h^m, G_h^c	1.20, 1.19	1.20, 1.05
Estimated / calculated from evolution data		IAA	DTA
Medial Smooth Muscle Gains (o)	$K_{M\sigma o}^m, K_{M\tau o}^m, K_{M\varphi o}^m$	0.473, 1.410, 0.010	0.140, 0.140, 0.210
Medial Collagen Gains (o)	$K_{M\sigma o}^c, K_{M\tau o}^c, K_{M\varphi o}^c$	0.550, 1.650, 0.012	0.800, 0.800, 1.230
Adventitial Collagen Gains (o)	$K_{A\sigma o}^c, K_{A\tau o}^c, K_{A\varphi o}^c$	0.331, 0.990, 0.007	12.21, 12.21, 18.78
Evolved Gains (h)	$K_{\Gamma\sigma h}^\alpha, K_{\Gamma\tau h}^\alpha, K_{\Gamma\varphi h}^\alpha$	$K_{\Gamma\sigma o}^\alpha, 0.033 \times K_{\Gamma\tau o}^\alpha, K_{\Gamma\varphi o}^\alpha$	$5 \times K_{\Gamma\sigma o}^\alpha, 5 \times K_{\Gamma\tau o}^\alpha, 5 \times K_{\Gamma\varphi o}^\alpha$
Mass Removal Rates (o)	$k_{M0o}^m, k_{M0o}^c, k_{A0o}^c$	$[1/10, 1/10, 1/10]$ day^{-1}	$[1/2, 1/16, 1/20]$ day^{-1}
Mass Removal Rates (h)	$k_{M0h}^m, k_{M0h}^c, k_{A0h}^c$	$[1/3, 1/3, 1/3]$ day^{-1}	$[2/3, 1/12, 1/15]$ day^{-1}

Table 1: Model parameters for both an original / basal (subscript o; control) and an evolved-to-new home-ostatic (subscript h; AngII infused) state for both the infrarenal abdominal aorta (IAA) and descending thoracic aorta (DTA) from $Apoe^{-/-}$ mice (Bersi et al. 2017). Parameters are separated by class: those prescribed based directly on measurements, those obtained via nonlinear regression of data, and those estimated based on prior G&R simulations and the ability to describe the time-course data available. "Elastin", "Muscle", and "Collagen" parameters represent elastin-dominated isotropic and smooth muscle / collagen-dominated anisotropic contributions, with glycosaminoglycans and other constituents not specified explicitly. Superscript $+$ or $-$ refer to behaviors in tension or compression; subscripts M and A refer to medial and adventitial respectively.
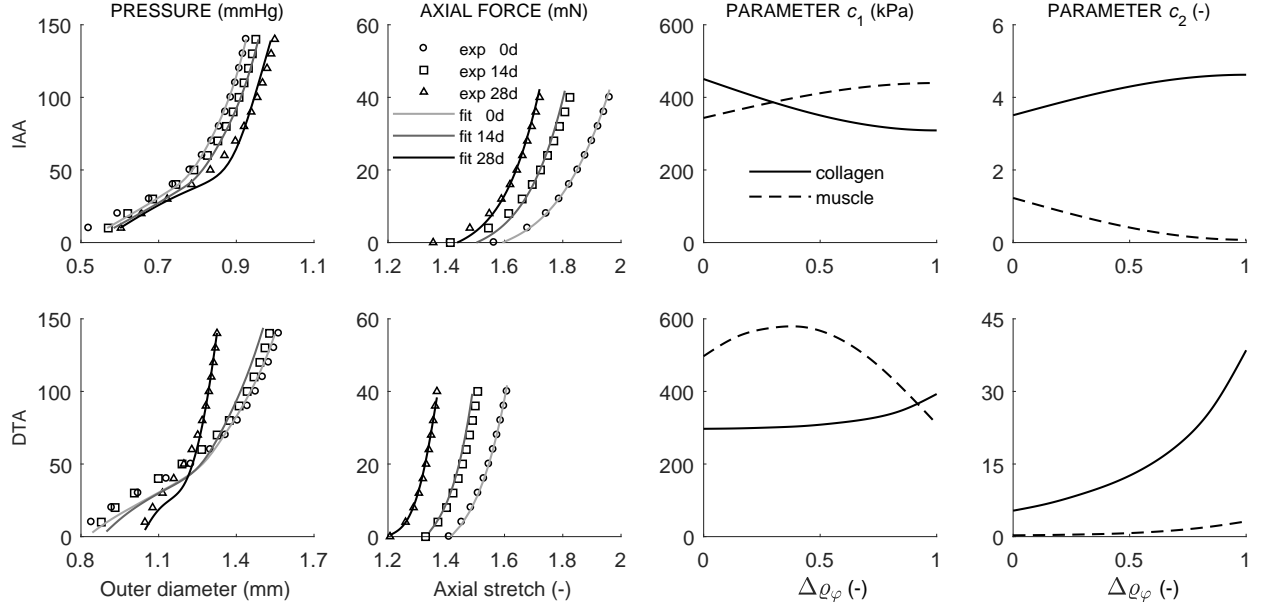
Figure 1: Columns one and two: Nonlinear regressions of mean pressure-diameter (at in vivo axial stretch and during unloading) and axial force-length (at luminal pressure of 100 mmHg and during unloading) experimental data (symbols), for the IAA (first row) and DTA (second row), computed with associated rate-independent G&R models (cf. Appendix 1 in Latorre and Humphrey 2018b). Albeit not shown, experimental tests at 7 and 21 days, as well as pressure-diameter tests at 0.95- and 1.05-fold axial stretches and force-length tests at 60 and 140 mmHg, were also included in the regression, with similar outcomes. Columns three and four: Evolution of best-fit model parameters in tension $c_1^{\alpha+}$ and $c_2^{\alpha+}$ for collagen ($\alpha = c$, solid line) and smooth muscle ($\alpha = m$, dashed line) as a function of the inflammatory cell burden $\Delta\varrho_\varphi$, as given by a progressive nonlinear regression. Note that $c_{1,2}^{\alpha+}(0) = c_{1,2o}^{\alpha+}$ and $c_{1,2}^{\alpha+}(1) = c_{1,2h}^{\alpha+}$, consistent with original (o) and evolved homeostatic (h) values in Table 1.
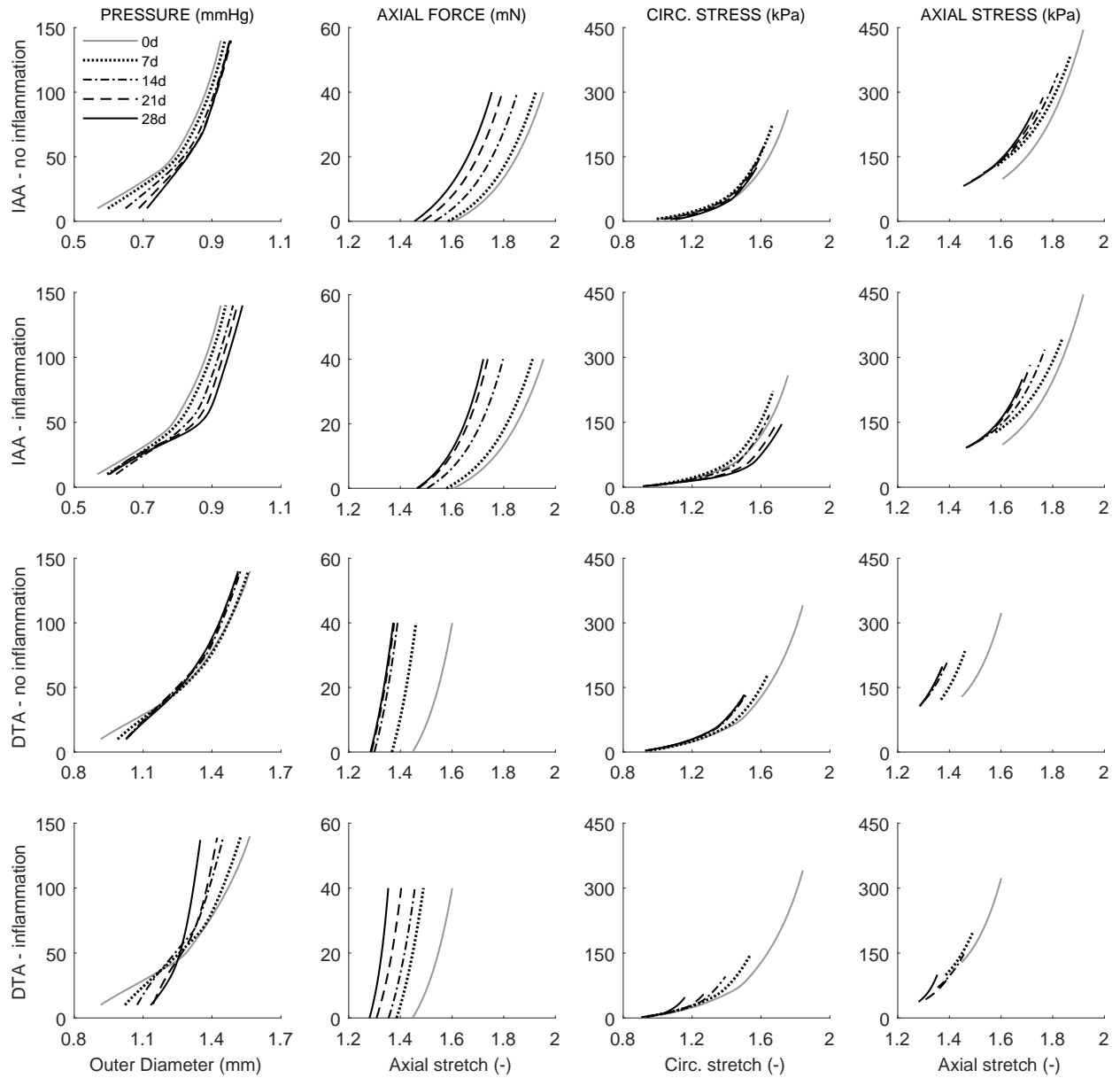
25

Figure 2: Model predictions of evolving passive biaxial mechanical responses with (second and fourth rows) or without (first and third rows) inclusion of the measured extents of inflammation. Pressure-diameter responses at individual values of in vivo axial stretch (first column) and axial force-length responses at a fixed luminal pressure of 100 mmHg (second column), as well as associated circumferential (third column) and axial (fourth column) Cauchy stress-stretch behaviors, for the IAA (first and second rows) and DTA (third and fourth rows) at baseline (0 days) and after 7, 14, 21, and 28 days of AngII infusion (cf. Figure S3 in Bersi et al. 2017).
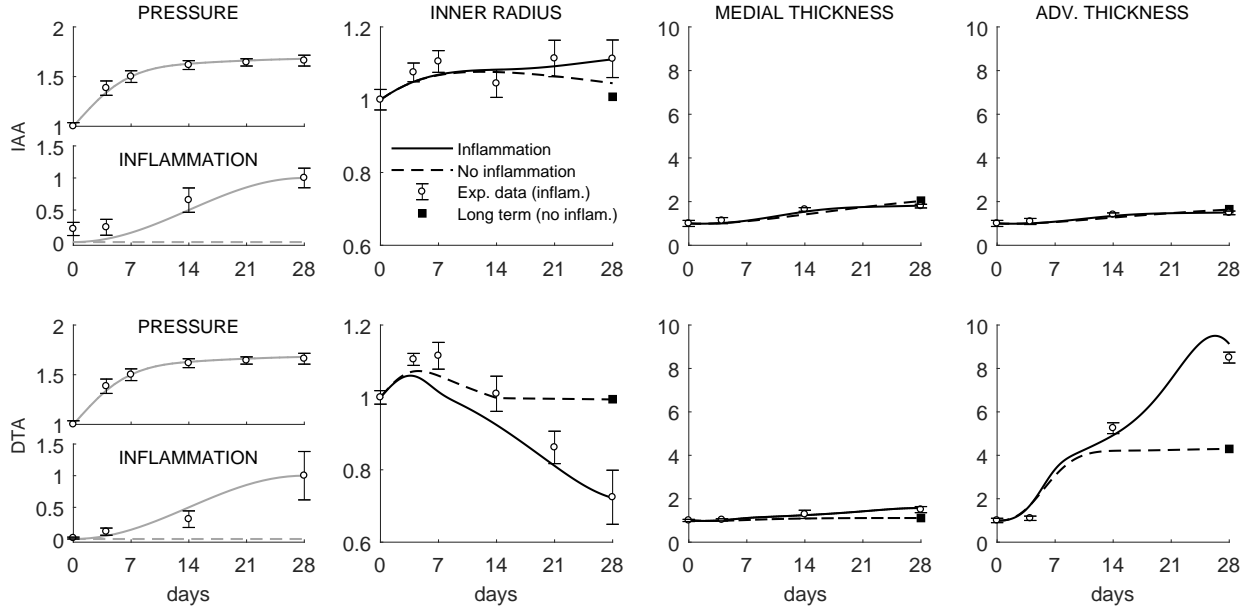
Figure 3: Model predictions of geometric (bilayered, with all quantities normalized to values at time 0 prior to AngII infusion) properties for the IAA (first row) and DTA (second row) following a rapid 1.68-fold increase in systolic pressure that persists up to $s = 28$ days (grey lines, model inputs). Predictions are shown with (black solid) or without (black dashed) inclusion of inflammatory effects, the former with a modest 4.9-fold increase in the IAA but a marked 67.6-fold increase in the DTA (respective grey lines, additional model inputs). Shown, too, are mean $\pm$ SEM experimental values (open circles with error bars) extracted from Bersi et al. (2017), as well as the associated mechanobiologically equilibrated (fully relaxed, at $s > 28$ days for IAA, but at $s \approx 14$ days for DTA) solution for the case with no inflammation and $P/P_o = 1.68$ (solid black square). Note a similar wall thickening in both cases in the IAA, although the luminal radius tends to return to normal in the simulation without inflammatory effects; note, too, a dramatic increase in adventitial versus medial thickening in the DTA after 14 days consistent with a delayed but exuberant production of inflammatory collagen within the adventitia.
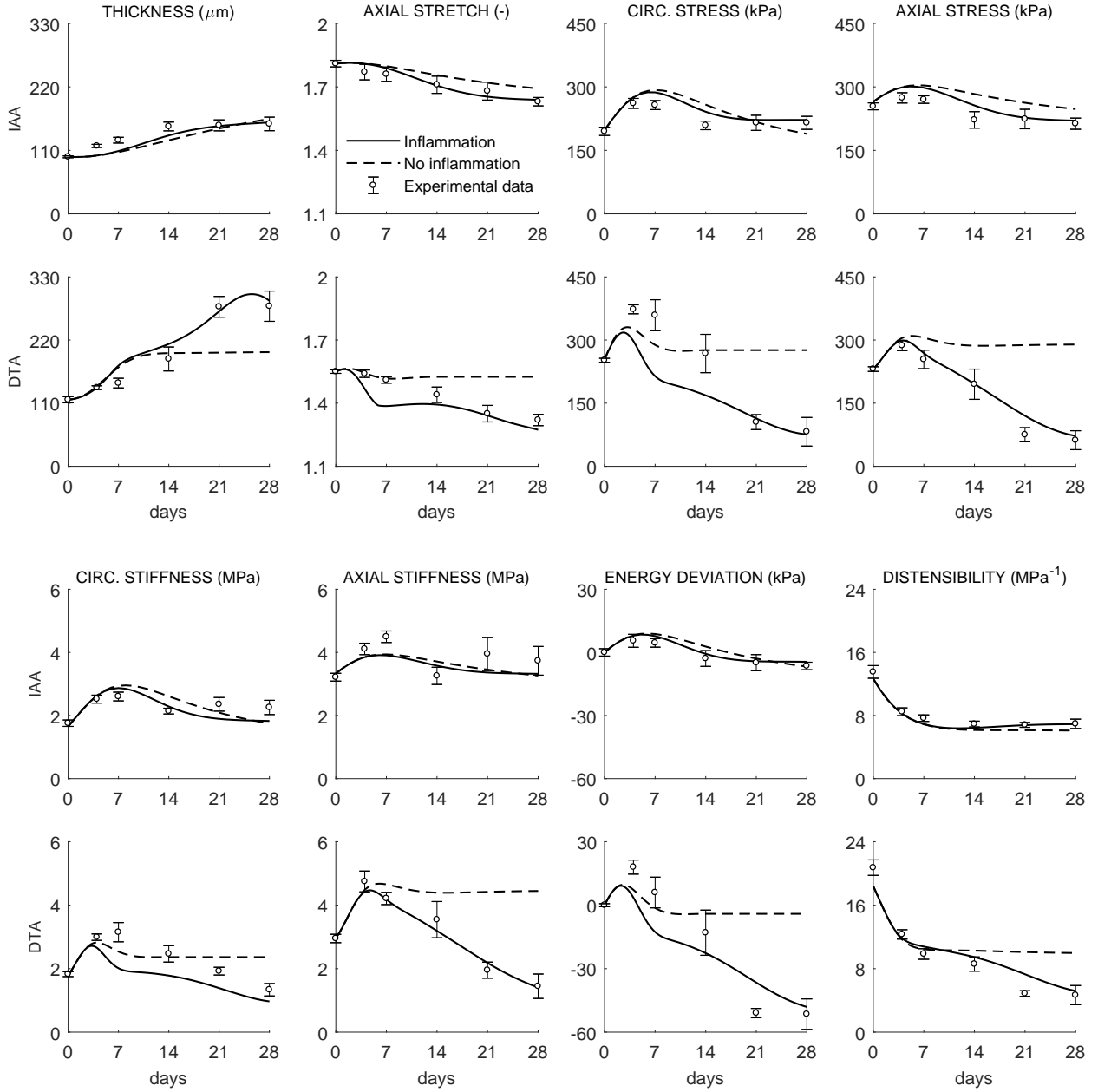
Figure 4: Evolving geometric, material and structural properties for the IAA (first and third rows) and DTA (second and fourth rows). Model predictions, with (solid) and without (dashed) inclusion of inflammatory effects, of (from left to right and top to bottom) wall thickness in unloaded traction-free configuration h^{tf} (μm), in-vivo axial stretch λ_z^{iv}, circumferential $\sigma_{\theta\theta}$ and axial σ_{zz} stress (kPa), circumferential $c_{\theta\theta\theta\theta}$ and axial c_{zzzz} stiffness (MPa), stored energy density per unit current volume relative to its value at time 0 prior to AngII infusion $W - W_o$ (to enable proper comparisons between energy functions with different referential values, cf. Eq. (S1) in Bersi et al., 2017), and distensibility $\mathcal{D}$ (MPa^{-1}) computed over time throughout AngII infusion at time-dependent systolic pressures (Figure 3). Symbols and error bars represent mean $\pm$ SEM experimental values (with inflammatory cell infiltration) at six times throughout the evolution: baseline (0 days), 4, 7, 14, 21 and 28 days (cf. Figure 1 in Bersi et al., 2017).
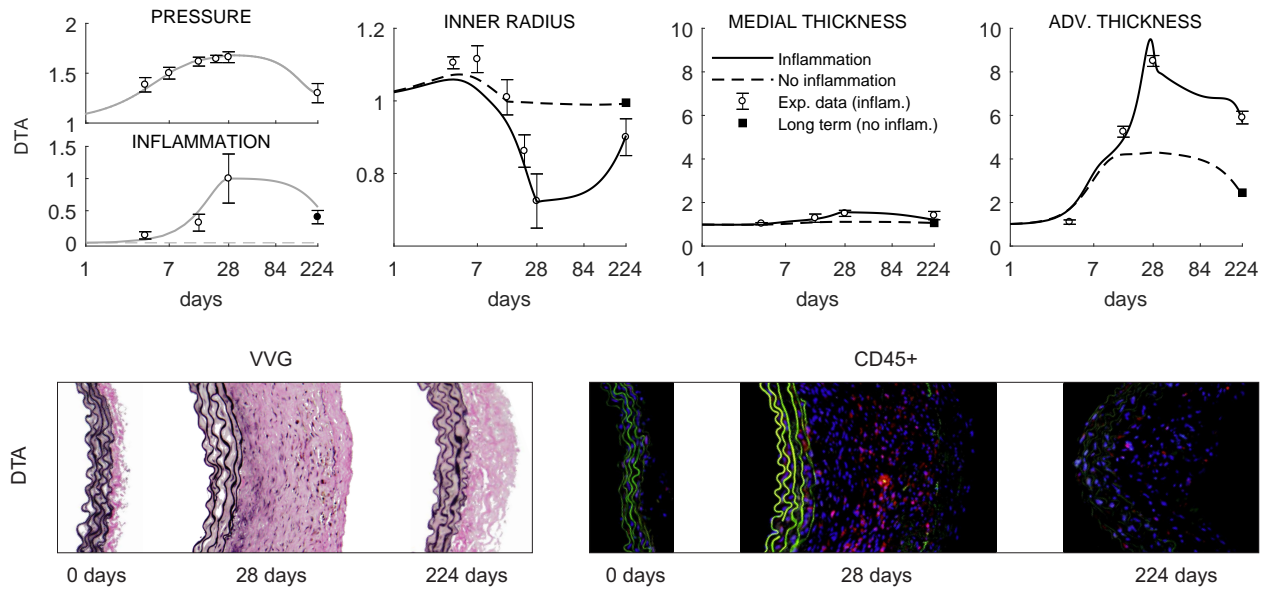
Figure 5: Top row: Model results for long-term responses – up to 196 days after terminating the AngII infusion at 28 days – of normalized geometric (bilayered) properties for the DTA following a 1.68-fold increase in systolic pressure (grey line, model input) that persists up to $s = 28$ days but drops to $P/P_o = 1.26$ during the subsequent 196 days (note the logarithmic scale starting at $s = 1$ day as well as the non-monotonic change in prescribed inflammation and computed geometry at $s = 28$ days). Predictions are shown with (black solid line) and without (black dashed line) inclusion of inflammatory effects that were measured up to 28 days (respective grey lines, additional model inputs). Shown, too, are mean ± SEM experimental values (open circles with error bars) extracted from Bersi et al. (2017), as well as the associated mechanobiologically equilibrated (adaptive, fully relaxed) solution for the case with no inflammation and $P/P_o = 1.26$ (solid black square). Note that the model predicted that some inflammatory effects needed to remain in order to describe the observed long-term, persistent maladaptive, response at 224 days. Bottom row: Based on this prediction, we examined available but previously unanalyzed histological sections (Verhoeff Van Gieson, or VVG, staining shows elastic fibers in black and collagen in pink; note the dramatic adventitial thickening due mainly to excessive collagen) and indeed found a continuing presence of inflammatory cells at 224 days (red immunostained CD45+ cells, a pan-inflammatory marker), which was quantified and is shown by the solid circle with error bar. This correspondence served as a further validation of the predictive capability of the model.